

Overhauser-enhanced magnetic resonance elastography

Najat Salameh^{a,b,c,d,*}, Mathieu Sarracanie^{a,b,c}, Brandon D. Armstrong^{a,c},
Matthew S. Rosen^{a,b,c,†} and Arnaud Comment^{d,†}

Magnetic resonance elastography (MRE) is a powerful technique to assess the mechanical properties of living tissue. However, it suffers from reduced sensitivity in regions with short T_2 and T_2^* such as in tissue with high concentrations of paramagnetic iron, or in regions surrounding implanted devices. In this work, we exploit the longer T_2^* attainable at ultra-low magnetic fields in combination with Overhauser dynamic nuclear polarization (DNP) to enable rapid MRE at 0.0065 T. A 3D balanced steady-state free precession based MRE sequence with undersampling and fractional encoding was implemented on a 0.0065 T MRI scanner. A custom-built RF coil for DNP and a programmable vibration system for elastography were developed. Displacement fields and stiffness maps were reconstructed from data recorded in a polyvinyl alcohol gel phantom loaded with stable nitroxide radicals. A DNP enhancement of 25 was achieved during the MRE sequence, allowing the acquisition of 3D Overhauser-enhanced MRE (OMRE) images with $(1.5 \times 2.7 \times 9)$ mm³ resolution over eight temporal steps and 11 slices in 6 minutes. In conclusion, OMRE at ultra-low magnetic field can be used to detect mechanical waves over short acquisition times. This new modality shows promise to broaden the scope of conventional MRE applications, and may extend the utility of low-cost, portable MRI systems to detect elasticity changes in patients with implanted devices or iron overload. Copyright © 2016 John Wiley & Sons, Ltd.

Keywords: MR Elastography (MRE); Electron Spin Resonance (ESR); ultra-low magnetic field; Overhauser MRI; iron overload; magnetic susceptibility

INTRODUCTION

Manual palpation of soft tissue is regularly performed by clinicians to detect changes in organs and glands, and remains the most efficient screening tool for breast cancer detection (1). Beginning in the late 1980s, new medical imaging techniques enabled remote palpation of regions not directly accessible by the hands of the examining physician. Ultrasound was the first modality to provide qualitative and quantitative evaluation of stiffness in soft tissue (2,3). Ultrasound has the advantage of being inexpensive and portable, making its use broader in clinical environments. However, acoustic impedance changes at interfaces (e.g. bones) limit the utility of ultrasound to applications in superficially accessible organs. Attenuation in tissue and in particular in fat impairs its use in obese patients. Finally, shear waves do not propagate in liquids, making its use in patients with ascites impossible.

Unlike ultrasound, magnetic resonance elastography (MRE) methods (4,5) provide information beyond tomographic measurement of elasticity, including high-resolution three-dimensional anatomical images, and wave attenuation related to the tissue viscosity. The latter cannot be neglected and has shown promising results in the diagnosis of non-alcoholic fatty liver diseases. Very interestingly, it was shown first in rodents and subsequently in humans that MRE can detect subjects with non-alcoholic steatohepatitis, even before fibrosis appears (6,7). Ultrasound and MR-based elastography are used routinely for the diagnosis of chronic hepatic diseases in multi-site studies. Consequently, and despite considerably longer acquisition times, interest in MR-based techniques for many applications is very high.

MRE has shown promising results for the diagnosis of chronic liver diseases (8–13), for discriminating between benign or malignant tumors in breast cancer patients (14), and for the screening of prostate cancer (15). MRE is currently under development for the investigation of brain disorders such as Alzheimer disease (16). If MRE methods could be performed at ultra-low magnetic field, it would extend the technique to cases

* Correspondence to: N. Salameh, Department of Radiology, A. A. Martinos Center for Biomedical Imaging, Massachusetts General Hospital, Charlestown, MA, USA. E-mail: najat.salameh@gmail.com

a N. Salameh, M. Sarracanie, B. D. Armstrong, M. S. Rosen
Department of Radiology, A. A. Martinos Center for Biomedical Imaging,
Massachusetts General Hospital, Charlestown, MA, USA

b N. Salameh, M. Sarracanie, M. S. Rosen
Department of Radiology, Harvard Medical School, Boston, MA, USA

c N. Salameh, M. Sarracanie, B. D. Armstrong, M. S. Rosen
Department of Physics, Harvard University, Cambridge, MA, USA

d N. Salameh, A. Comment
Institute of Physics of Biological Systems, École Polytechnique Fédérale de
Lausanne, Lausanne, Switzerland

† These authors contributed equally to this work.

Abbreviations used: MRE, magnetic resonance elastography; OMRE, Overhauser-enhanced magnetic resonance elastography; bSSFP, balanced steady-state free precession; DNP, dynamic nuclear polarization; SNR, signal-to-noise ratio; MSG, motion-sensitizing gradient; TEMPOL, 4-hydroxy-2,2,6,6-tetramethylpiperidine 1-oxyl; PVA, polyvinyl alcohol; ESR, electron spin resonance; OD, outer diameter; ID, inner diameter; ULF, ultra-low field

where magnetic susceptibility currently precludes it, such as iron overload liver disease, and regions adjacent to implanted devices.

The implementation of MRE is a three-step process of (1) wave generation, (2) acquisition of dynamic motion-sensitized MRI, and (3) signal deconvolution to extract the mechanical properties of tissue from the MR images. The first step is generally achieved using an external driver (acoustic, pneumatic, piezoelectric, or electromechanical transducer) that generates steady-state shear or transverse waves. Second, traditional MRI acquisition sequences are employed with motion-sensitizing gradients (MSGs) added to record phase contrast images. Images are processed to extract wave propagation. Finally, from the processed phase images – called displacement field maps – an inversion algorithm (14) is used to calculate the shear mechanical properties. Although robust, MRE, and more generally MRI, suffers from inherently low signal-to-noise ratio (SNR) in the presence of magnetic susceptibility gradients such as in subjects with implanted devices or iron overload, owing to shortened T_2^* . The addition of MSG to an imaging sequence increases the echo time (T_E), leading to a further decrease in NMR sensitivity to short T_2 species. Signal averaging can, to some extent, compensate for the reduction of sensitivity but at the expense of increasing acquisition times. This problem is further exacerbated in high field scanners (1.5 T and above), as artifacts from magnetic susceptibility gradients increase with increasing field strength. These artifacts make diagnosis difficult or impossible in these cases.

Iron overload is found in up to 56% of patients with chronic liver disease (17). A 5% failure rate has been reported for MRE due to severe iron deposition in the liver that dramatically reduced the signal intensity of the NMR images (18). In 2001, Weaver *et al.* sensitized MRE users to the impact of low SNR on the calculation of the elastograms (19). SNR impairment will not prevent the acquisition of an MR image but this reduction in SNR leads to a drop in phase sensitivity that can lead to underestimating the mechanical properties of the tissue under study. To the best of our knowledge, no systematic evaluation of the errors appearing in elastograms due to decreased SNR (and thus phase errors) has been performed to date. With poor SNR, the MRE examination thus does not formally “fail”, but the accuracy of the final diagnosis will be adversely affected. Currently, the only alternatives to situations where insufficient SNR precludes MRE are ultrasound, which has lower reliability than MRE (75% as reported by Yoon *et al.* (18), X-ray based modalities (such as CT), or invasive (and potentially risky) surgical biopsy (20,21). So there exists a clear need for non-ionizing, non-invasive MRE imaging strategies at lower magnetic field strengths.

In the present work, we show the feasibility of performing MRE at very low magnetic field, where long T_2^* resulting from reduced magnetic susceptibility (22) enables longer readout times, even in the presence of paramagnetic iron. We combine ultra-low-field MRI at 0.0065 T with *in situ* Overhauser dynamic nuclear polarization (DNP) to boost the MR signal. Overhauser DNP (23) can increase the NMR signal by up to two orders of magnitude above thermal equilibrium using stable nitroxide radicals (24) in a simple double-resonance setup. Overhauser DNP is well suited to low magnetic field strength as the penetration depth of the electron saturation pulse is greater at lower frequencies, and sample heating is reduced as the specific absorption rate is proportional to ω^2 . This proof of concept experiment is the first step toward *in vivo* preclinical applications of Overhauser-enhanced MRE (OMRE).

METHODS

Phantom preparation

A 7%-PVA (polyvinyl alcohol) gel containing 5 mM 4-hydroxy-2,2,6,6-tetramethylpiperidine 1-oxyl (TEMPOL) dissolved in water (Sigma-Aldrich, St. Louis, MO, USA) was obtained by two cycles of freezing–thawing at -20°C and room temperature (25). The gel was placed in a 5.5 cm inner diameter (ID), 6.0 cm outer diameter (OD), and 10.0 cm long 3D-printed cylindrical holder made of polycarbonate (Fig. 1). T_1 and T_2 relaxation times of the MRE phantom were obtained with conventional inversion recovery and Carr–Purcell–Meiboom–Gill spectroscopic measurements at 6.5 mT: $T_1 = 200 \pm 2$ ms; $T_2 = 156 \pm 2$ ms.

Ultra-low-field (ULF) MRI scanner and coil design

MRE was performed in a custom-built ULF MRI scanner consisting of a bi-planar 6.5 mT electromagnet with bi-planar gradients, as previously described in Reference (26) and shown in Figure 1. A Redstone MRI console (Tecmag, Houston, TX, USA) was used for sequence programming, data acquisition, and hardware (gradient and RF amplifiers) control. MR signal enhancement was obtained using Overhauser DNP at 6.5 mT. Two coils were used: a 10 cm OD 16 cm long solenoid coil for NMR excitation and detection at 276 kHz, and a 7 cm OD 13 cm long Alderman–Grant resonator for electron spin resonance (ESR) irradiation at 140.8 MHz as described in Reference (27). The ESR coil was placed inside the NMR coil. SNR in the motion-encoded images was calculated using the ratio between

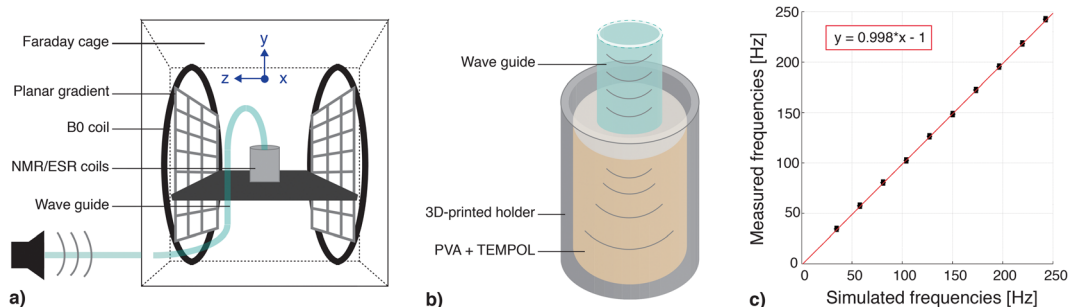


Figure 1. (a) Schematic diagram of the experimental setup. A loudspeaker is placed outside of the Faraday cage and generates pressure waves guided via a tube in contact with the PVA gel. (b) The phantom is positioned inside of a 3D-printed cylindrical holder, itself inside of the NMR and ESR coils. (c) The measured resonances of the vibrating system are plotted versus the calculated resonances. A linear fit (red line) and its equation are shown on the plot.

the mean signal magnitude over the whole phantom volume and the standard deviation of a user-defined noise region on each dataset.

Wave generation

Acoustic pressure waves were generated by a 30 cm diameter loudspeaker (B&C Speakers, Pompton Plains, NJ, USA) located outside of the Faraday cage enclosing the low-field scanner (see Fig. 1(a)). A 7.4 m long 22 mm ID tube was used to guide the acoustic waves into the scanner. The extremity of the tube was closed with a flexible rubber membrane positioned on top of the investigated gel (Fig. 1(b)). The resonance frequencies f_n of the system are given by

$$f_n = \frac{n + 1/2}{2L} c_a \quad [1]$$

where L is the length of the tube, c_a the speed of sound in air, and n is an integer. A similar system has previously been described and validated *in vivo*, showing good reproducibility in rat brains (28). The computed resonances were experimentally validated with a microphone (error ± 1 Hz) by sweeping the frequency from 1 to 250 Hz. Computed resonances were compared with measured frequencies (Fig. 1(c)). Longitudinal waves were transmitted to the gel using this setup.

Ultra-low-field MRE sequence

To compensate for our lack of NMR sensitivity in the ULF regime, signal averaging is necessary. In order to avoid prohibitively long acquisition times, fast acquisition strategies were employed to accelerate imaging. A 3D balanced steady-state free precession (bSSFP)-based sequence (29) was combined with fractional encoding for MRE, and undersampling schemes with variable density Gaussian patterns as described in Reference (27) were also used. bSSFP sequences allow the highest SNR per unit time by pulsing rapidly without waiting for T_1 recovery (29). A steady state is reached after a short number of pulses, and the transverse magnetization is maximal for $T_2/T_1 \sim 1$ (29), similar to the regime observed at ULF. Fractional encoding allows encoding the motion at a frequency (f_G) higher than the driving frequency

for the vibrations (f_v), significantly reducing the time per T_R needed for motion encoding. The phase accumulation obtained with this technique is described by the following equation (30,31):

$$\Phi = \frac{\gamma G A_{\text{tot}} \sin(\pi q)}{f_G \pi (1 - q^2)}, \quad [2]$$

where q is the ratio between the vibration frequency f_v and the MSG frequency f_G , γ the gyromagnetic ratio, A_{tot} the displacement amplitude, and G the gradient amplitude.

The motion sensitivity of our ULF scanner (with imaging gradient strength of the order of 1 mT/m) was simulated and compared with a conventional high-field clinical scanner with gradients ranging from 20 to 30 mT/m (31) (see Fig. 2(a)). This comparison reflects only the motion sensitivity efficiency and not differences in SNR. The addition of SNR considerations to Equation [2] allows us to assess the minimum displacement our 6.5 mT system can detect given the error on the phase images ($\text{err} = 1/\text{SNR}$ (32)).

Simulations were performed with one MSG alternatively positioned on the three spatial axes: X (read direction), Y (3D phase encode direction), and Z (2D phase encode direction) (see Fig. 2(b)). Transverse magnetization using T_1 and T_2 measured in our MRE phantom was calculated using a MATLAB-based Bloch equation solver for a bSSFP-based sequence with varying flip angle and off-resonance values due to B_0 inhomogeneities. Results are shown in Figure 3(a).

The imaging parameters were the following: matrix size = $(65 \times 64 \times 11)$, resolution = $(1.5 \times 2.7 \times 9)$ mm³, $T_E/T_R = 24/39$ ms, $\alpha = 90^\circ$, and $\text{NA} = 1$. The flip angle used here was the optimal one as determined in the simulations described above.

Eight temporal steps evenly distributed over one period of the acoustic excitation were acquired, leading to an acquisition time of 111.5 s per spatial direction. One additional scan was performed with the transducer turned off and served as a reference for B_0 drift correction. A total ESR irradiation time of 28 ms/ T_R was used to drive Overhauser DNP. As shown in Figure 2(b), ESR irradiation was included within each T_R , consisting of a significant source of acceleration compared with conventional OMRI sequences, which usually require long

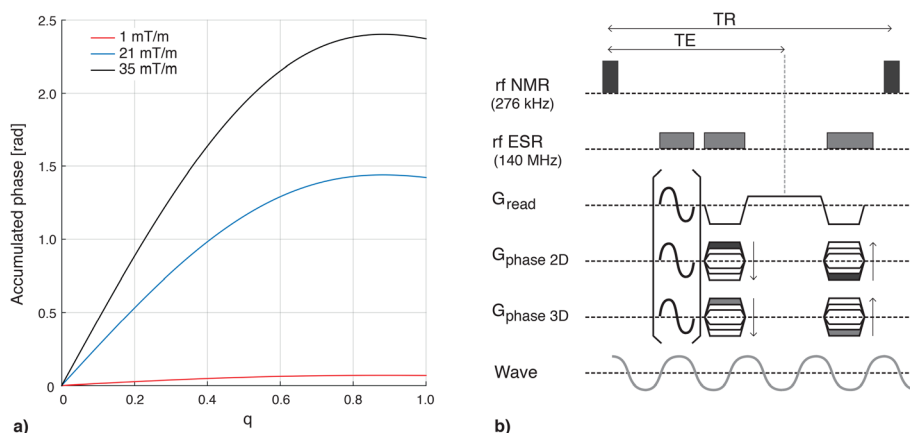


Figure 2. (a) Accumulated phase simulated for three different encoding gradient strengths. Simulation parameters: $f_G = 206$ Hz (frequency used in our study), $A_{\text{tot}} = 100$ μm , $G = 1$ mT/m (typical in the ULF scanner), $G = 21$ mT/m (31), and $G = 35$ mT/m (30). (b) Diagram of the MRE sequence. The MSGs are placed before the encoding steps. The ESR irradiation is performed during the MSG, the phase encoding steps, and the delay between phase rewinders and the next RF pulse. The excitation wave is triggered with the imaging sequence, and its driven frequency is different from the MSG frequency.

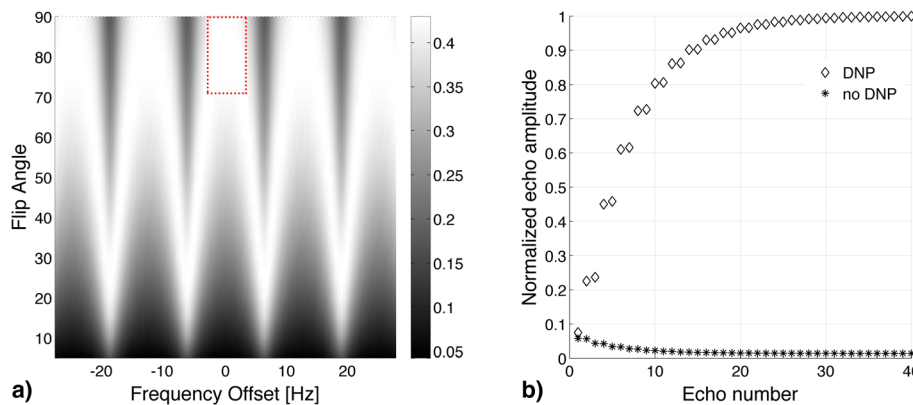


Figure 3. (a) Imaging parameter optimization. For T_1 and T_2 of our phantom, Bloch equation simulations led to an optimum flip angles in the range of 70–90° on resonance (red dotted rectangle). (b) Simulations with ESR irradiation embedded in imaging sequence, $\alpha = 90^\circ$, and relaxation times of our phantom show that 90% of the steady-state polarization value is reached after 14 echoes (~546 ms).

prepolarization pulses for each T_R before the MRI acquisition starts. Bloch simulations were performed to model the transverse magnetization approach to steady state in this interleaved hyperpolarization–acquisition scheme, and estimate the maximum signal enhancement due to the Overhauser effect (27). The input parameters for the simulation are the measured T_1 and T_2 relaxation times, the measured maximum enhancement obtained with an ESR pulse width of five times the proton T_1 of the sample in a 1D spectroscopy experiment (–30-fold enhancement), $T_E/T_R = 24/39$ ms, and $\alpha = 90^\circ$. The 1D enhancement factor was measured by calculating the SNR ratio between the Overhauser DNP experiment and the same experiment at thermal equilibrium.

Image reconstruction and data processing

k -space in the phase encode directions was randomly undersampled using a variable density Gaussian pattern to reduce acquisition time (27). The variable density Gaussian sampling was tuned to emphasize the center of k -space while maintaining acquisition of higher spatial frequencies to prevent image blurring. Random undersampling was used to prevent coherent artifacts in the reconstructed images. The missing lines in the undersampled k -space were filled with zeros; no other processing was added before Fourier transformation. We first evaluated the impact of undersampling on the displacement fields. For this purpose, MRE data acquired with 25, 50, and 75% sampling was compared with full k -space sampling. Each dataset was corrected for B_0 drift and unwrapped before comparison. The undersampling rate that resulted in the minimum acquisition time with the best motion sensitivity was then used for acquisitions using the fractional encoding approach as described in the previous section.

Viscoelastic maps were calculated using previously described methods (33). For each dataset, phase images were unwrapped using a Laplacian unwrapping algorithm (34) and corrected for B_0 drift. Phase maps were obtained by subtracting the reference unwrapped phase from the unwrapped phase images acquired for each direction with vibrations turned on. Three-dimensional convolution filtering was applied to the resulting phase maps with a Gaussian kernel using the `filter2` function from MATLAB. The curl operator was then applied in order to remove all contribution from compressional waves and to be left with pure shear displacements. The amplitude and phase of the wave

in each direction were locally assessed after Fourier transformation in the time domain and demodulation at the excitation frequency. The equation of motion was finally inverted to calculate locally the isotropic complex shear modulus G^* (14):

$$-\rho(2\pi f\nu)^2 \mathbf{u} = \mathbf{G}^* \cdot \nabla^2 \mathbf{u}, \quad [3]$$

where ρ is the density of the phantom (equal to water density), \mathbf{u} the curl of the displacement field, ∇^2 the Laplacian operator, and $\mathbf{G}^* = G_d + iG_l$ (G_d being the dynamic or storage modulus, and G_l the loss modulus).

All data was processed with MATLAB (MathWorks, Natick, MA, USA) scripts written in house.

RESULTS

The calculated mechanical resonances of the system are in excellent agreement with the measured resonances ($r^2 = 0.998$), as illustrated in Figure 1(c). The fourth-order harmonic resonance corresponding to a 103 Hz acoustic wave was chosen as the operational frequency for vibration, f_v .

The simulated approach to steady state of the transverse magnetization shows that the signal rapidly builds up to 25 times that of the thermal equilibrium signal (Fig. 3(b)). The build-up time constant corresponds to the T_1 relaxation time constant of the sample (200 ms). It was deduced from the Bloch simulations that the signal reaches about 90% of its steady-state value after 546 ms, corresponding to 14 echoes.

The influence of undersampling on unwrapped phase images is shown in Figure 4. A line was drawn crossing the entire gel and the corresponding normalized profile was recorded. The periodicity of the propagating wave was the same whatever sampling percentage was used. However, the peak-to-peak amplitude was about 40% lower for 25% sampling and remained close to what is observed for full sampling when sampling 75 or 50% of k -space (a maximum of 10% variation was observed). We therefore chose 50% undersampling for the rest of the study.

Over the different temporal steps, regions of interest enclosing the entire gel section of each slice were drawn in the phantom images, and the corresponding mean SNR for the entire volume was 39.8 ± 8.7 . The error on the phase calculated from mean SNR and Equation [2] led to a minimum motion

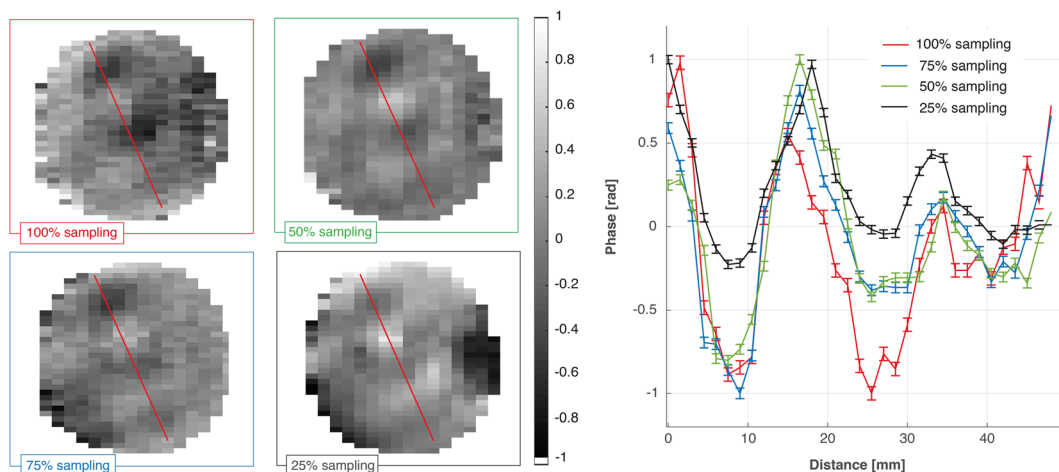


Figure 4. Effect of undersampling strategies on phase accumulation. Left: unwrapped phases for full sampling, 75%, 50%, and 25% sampling on one slice. Right: corresponding normalized profiles of the line drawn across the gel (in red).

sensitivity of 45 μm . The waves propagate over the entire volume and the total mean peak-to-peak total displacement was 1.47 ± 0.49 mm.

The storage (G_d) and loss (G_l) moduli of one slice are shown in Figure 5. Mean G_d and G_l and standard deviations across this same slice were calculated to be $G_d = 2.3 \pm 1.0$ kPa and $G_l = 1.9 \pm 0.9$ kPa.

DISCUSSION

We have shown for the first time that Overhauser DNP can be used to increase the sensitivity of MRE at ultra-low magnetic field. A total 3D acquisition time for eight temporal steps in 6 min was achieved, providing opportunity for magnetic susceptibility artifact-free MRE. “Snapshots” of the acoustic wave propagating across a PVA-gel with 5 mM TEMPOL were acquired with $\text{SNR} = 39.8 \pm 8.7$ and mean total wave amplitude of 1.47 ± 0.49 mm. Displacements are measurable along the entire gel (10 cm), meaning that the current transducer system can be used reliably to transmit longitudinal waves through soft materials and in particular tissue with a depth that is commensurate with the size of small animals. From our experience, the displacement field map quality is sufficient to consider a transfer to *in vivo* applications.

Our total acquisition time is 6 minutes at 6.5 mT. By way of comparison, the pioneering work of Muthupillai *et al.* (5) demonstrated MRE at 1.5 T with a minimum acquisition time of 10 s for a single temporal step and encoding direction, over a single 10 mm thick slice. If one considers that we have an equivalent SNR and spatial resolution, the fastest case Muthupillai *et al.* described in 1995 with imaging parameters equivalent to ours (i.e. the same number of temporal steps, slices, phase-encode steps, and 3D motion encoding) would require a 5.5 minutes acquisition even with B_0 about 230 times higher than ours. Our time saving comes from the use of fast imaging strategies initially designed for high-field MRI and used in our laboratory (26), combined with Overhauser DNP (27) as well as modern elastography techniques such as fractional encoding (30,31), and adapted to the ultra-low-field regime. This work reports for the first time MRE at field strengths well below 1.5 T.

The complex modulus was calculated from MRE data, and the storage modulus was found to be in the same range as described in the literature (35), although slightly smaller. This may be due to the fact that we are operating at a different vibration frequency (rheometry versus MRE, with storage modulus being frequency dependent), or due to the addition of free radicals to the initial preparation, which might impact the polymerization of PVA in solutions.

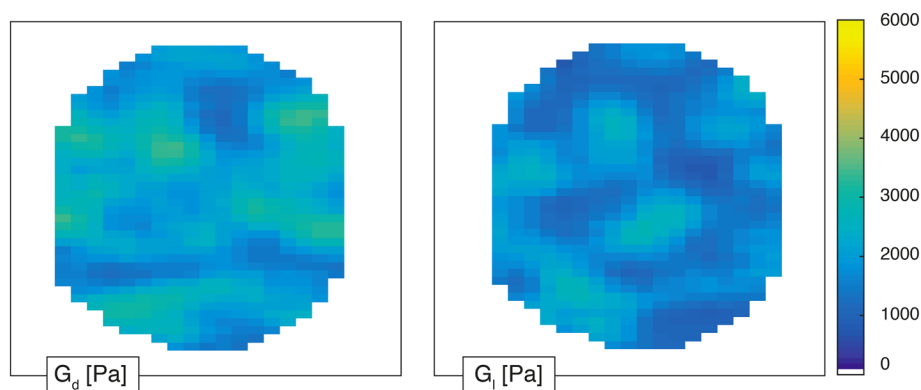


Figure 5. G_d and G_l for one slice. The mean G_d and G_l and standard deviation across this slice were calculated to be $G_d = 2.3 \pm 1.0$ kPa and $G_l = 1.9 \pm 0.9$ kPa.

To determine the increase in signal due the Overhauser effect, a single pulse, 1D spectroscopy experiment was performed. The signal magnitude of the gel with ESR was compared with the signal magnitude without ESR. The enhanced signal was 30 times larger than without using the Overhauser effect. Because the ESR irradiation is turned off during acquisition, this represents an upper limit to the signal enhancement during MRE experiments. The simulations showed that the embedded ESR irradiation in the MRE sequence successfully produced a 25-fold enhancement. Here, the steady-state enhancement we attain approaches the maximum obtainable on a 1D single-pulse spectroscopic experiment. This result indicates high polarization efficiency of the embedded ESR scheme in the imaging sequence.

As expected from operation at more than 20 times lower gradient strength with respect to clinical scanners, our sensitivity to motion is not as high as in state-of-the-art high-magnetic-field MRE. Nonetheless, it is sufficient for hepatic MRE (36). In order to further increase motion sensitivity in our system, straightforward solutions exist to improve the current protocol. Higher-amplitude pressure waves will translate to motion sensitivity gain. This can be achieved by improvement in the coupling between the waveguide and the phantom and by using a more rigid waveguide, causing less attenuation of the acoustic wave. In addition, limitations in the ULF scanner gradient set currently restrict both the maximal spatial and motion resolution. Equation [2] shows that the phase sensitivity to displacement is linearly proportional to the gradient amplitude. Thus, increasing the imaging gradient amplitude from its current value of about 1 mT/m to 2 mT/m will double our efficiency. Higher increase in gradient strength is also possible if the main magnetic field is increased as well in order to reduce concomitant field effects, which would result in image distortion. A three to four times higher motion sensitivity could be obtained with B_0 twice as high (13 mT) and gradients of the order of 3–4 mT/m. Such a configuration would permit a threefold increase in SNR due to the increase in field strength (37), or similarly a 3²-fold reduction of the total acquisition time.

OMRI is already performed in small animals, and shows promising results in the study of proteolytic activity, causing no harm to the animal (38), as well as in the study of oxidative stress in a rat model of brain ischemia–reperfusion (39), and without significant overheating. This became feasible owing to our fast imaging approach (27). In the context of OMRE, a few adaptations of the current setup need to be made for *in vivo* experiments. First, new coil designs with a better filling factor for NMR detection, and more localized ESR transmission to the liver, will be built. Second, the coupling between the waveguide and the animal will be optimized according to anatomical constraints. Third, motion compensation will certainly be necessary due to bulk motion from respiration. Finally, issues related to the *in vivo* reactivity of nitroxide radicals may be alleviated by using the low-toxicity long *in vivo* half-life triarylmethyl radicals developed for *in vivo* oximetric imaging (40,41). Doses in the literature range from less than 1 mM to a few tens of millimolar of free radicals. The intravenous route will certainly be preferred in order to have fast uptake in the liver and reduce the effect of radicals being scavenged by metabolic processes before reaching the targeted organs. The hardware improvements described above will improve imaging efficiency, permitting either faster acquisitions or the use of reduced nitroxide concentration. A compromise between acquisition time and free radical concentration

would allow a safer transfer to *in vivo* applications. Overall, low-field MRE could provide a simple and portable system for detection of elasticity changes in subjects with iron overload or implanted devices.

CONCLUSION

We have demonstrated that MRE can be performed in combination with Overhauser DNP at ultra-low magnetic field. This result may open new perspectives in the diagnosis of chronic liver diseases in subjects with iron overload if validated *in vivo*. At high magnetic field, MRI is currently used to detect and quantify the iron level in these patients, but is not used to perform dynamic functional imaging, as the signal in the liver drops dramatically due to its very short T_2^* . One-dimensional transient elastography has shown that elasticity is not affected by iron overload to stage fibrosis in patients with hemochromatosis (42,43). This result encourages alternative work with MR, which offers, as opposed to traditional ultrasound techniques, three-dimensional access to the organ, as well as information linked to wave attenuation, and thus viscosity, without suffering from the presence of water (ascites), fat and/or bones. Because MRE has also shown promising results in screening non-alcoholic steato-hepatitis subjects at risk of developing fibrosis (6,7), this novel technique has the potential to become a valuable non-invasive alternative to biopsy for patients with chronic liver diseases and iron overload.

Acknowledgements

This work was supported by the Swiss National Science Foundation (P300P2_147768 and PP00P2_133562), and by the Department of Defense, Defense Medical Research and Development Program, Applied Research and Advanced Technology Development Award W81XWH-11-2-0076 (DM09094).

REFERENCES

- 1 Goodson WH, III. Clinical breast examination. *West. J. Med.* 1996; 164: 355–358.
- 2 Madsen EL, Sathoff HJ, Zagzebski JA. Ultrasonic shear wave properties of soft tissues and tissuelike materials. *J. Acoust. Soc. Am.* 1983; 74: 1346–1355.
- 3 Krouskop TA, Dougherty DR, Vinson FS. A pulsed Doppler ultrasonic system for making noninvasive measurements of the mechanical properties of soft tissue. *J. Rehabil. Res. Dev.* 1987; 24: 1–8.
- 4 Plewes DB, Betty I, Urchuk SN, Soutar I. Visualizing tissue compliance with MR imaging. *J. Magn. Reson. Imaging* 1995; 5: 733–738.
- 5 Muthupillai R, Lomas D, Rossman P, Greenleaf J, Manduca A, Ehman R. Magnetic resonance elastography by direct visualization of propagating acoustic strain waves. *Science* 1995; 269: 1854–1857.
- 6 Salameh N, Larrat B, Abarca-Quinones J, Pallu S, Dorvillius M, Leclercq I, Fink M, Sinkus R, Van Beers BE. Early detection of steatohepatitis in fatty rat liver by using MR elastography. *Radiology* 2009; 253: 90–97.
- 7 Chen J, Talwalkar JA, Yin M, Glaser KJ, Sanderson SO, Ehman RL. Early detection of nonalcoholic steatohepatitis in patients with nonalcoholic fatty liver disease by using MR elastography. *Radiology* 2011; 259: 749–756.
- 8 Huwart L, Peeters F, Sinkus R, Annet L, Salameh N, Beek ter LC, Horsmans Y, Van Beers BE. Liver fibrosis: non-invasive assessment with MR elastography. *NMR Biomed.* 2006; 19: 173–179.
- 9 Huwart L, Sempoux C, Salameh N, Jamart J, Annet L, Sinkus R, Peeters F, ter Beek LC, Horsmans Y, Van Beers BE. Liver fibrosis: noninvasive assessment with MR elastography versus aspartate aminotransferase-to-platelet ratio index. *Radiology* 2007; 245: 458–466.
- 10 Huwart L, Sempoux C, Vicaut E, Salameh N, Annet L, Danse E, Peeters F, ter Beek LC, Rahier J, Sinkus R, Horsmans Y, Van Beers BE. Magnetic

- resonance elastography for the noninvasive staging of liver fibrosis. *Gastroenterology* 2008; 135: 32–40.
- 11 Yin M, Talwalkar JA, Glaser KJ, Manduca A, Grimm RC, Rossman PJ, Fidler JL, Ehman RL. Assessment of hepatic fibrosis with magnetic resonance elastography. *Clin. Gastroenterol. Hepatol.* 2007; 5: 1207–1213.e2.
 - 12 Rouvière O, Yin M, Dresner MA, Rossman PJ, Burgart LJ, Fidler JL, Ehman RL. MR elastography of the liver: preliminary results. *Radiology* 2006; 240: 440–448.
 - 13 Asbach P, Klatt D, Hamhaber U, Braun J, Somasundaram R, Hamm B, Braun J, Sack I. Assessment of liver viscoelasticity using multifrequency MR elastography. *Magn. Reson. Med.* 2008; 60: 373–379.
 - 14 Sinkus R, Siegmann K, Xydeas T, Tanter M, Claussen C, Fink M. MR elastography of breast lesions: understanding the solid/liquid duality can improve the specificity of contrast-enhanced MR mammography. *Magn. Reson. Med.* 2007; 58: 1135–1144.
 - 15 Nir G, Sahebjavaher RS, Kozlowski P, Chang SD, Sinkus R, Goldenberg SL, Salcudean S. Model-based registration of ex vivo and in vivo MRI of the prostate using elastography. *IEEE Trans. Med. Imaging* 2013; 32: 1349–1361.
 - 16 Schregel K, Tysiak EWN, Garteiser P, Gemeinhardt I, Prozorovski T, Aktas O, Merz H, Petersen D, Wuerfel J, Sinkus R. Demyelination reduces brain parenchymal stiffness quantified in vivo by magnetic resonance elastography. *Proc. Natl. Acad. Sci. U. S. A.* 2012; 109: 6650–6655.
 - 17 Deugnier Y, Turlin B. Pathology of hepatic iron overload. *World J. Gastroenterol.* 2007; 13: 4755–4760.
 - 18 Yoon JH, Lee JM, Joo I, Lee ES, Sohn JY, Jang SK, Lee KB, Han JK, Choi BI. Hepatic fibrosis: prospective comparison of MR elastography and US shear-wave elastography for evaluation. *Radiology* 2014; 273: 772–782.
 - 19 Weaver JB, Van Houten EE, Miga MI, Kennedy FE, Paulsen KD. Magnetic resonance elastography using 3D gradient echo measurements of steady-state motion. *Med. Phys.* 2001; 28: 1620–1628.
 - 20 Castéra L, Nègre I, Samii K, Buffet C. Pain experienced during percutaneous liver biopsy. *Hepatology* 1999; 30: 1529–1530.
 - 21 Thampanitchawong P, Piratvisuth T. Liver biopsy: complications and risk factors. *World J. Gastroenterol.* 2007; 13: 4755–4760.
 - 22 Salameh N, Sarracanie M, Farrar C, Waddington DE, Zhu B, Comment A, Rosen MS. MR elastography in the presence of iron overload. *Proceedings of the 23rd Annual Meeting ISMRM*, Toronto, 2015; 1060.
 - 23 Overhauser A. Polarization of nuclei in metals. *Phys. Rev.* 1953; 92: 411–415.
 - 24 Armstrong BD, Han S. A new model for Overhauser enhanced nuclear magnetic resonance using nitroxide radicals. *J. Chem. Phys.* 2007; 127: 104508.
 - 25 Mano I, Goshima H, Nambu M, Iio M. New polyvinyl alcohol gel material for MRI phantoms. *Magn. Reson. Med.* 2005; 3: 921–926.
 - 26 Sarracanie M, LaPierre CD, Salameh N, Waddington DEJ, Witzel T, Rosen MS. Low-cost high-performance MRI. *Sci. Rep.* 2015; 5: 15177.
 - 27 Sarracanie M, Armstrong BD, Stockmann J, Rosen MS. High speed 3D Overhauser-enhanced MRI using combined b-SSFP and compressed sensing. *Magn. Reson. Med.* 2013; 71: 735–745.
 - 28 Salameh N, Souris L, Sarracanie M, de Rochefort L, Sinkus R, Darrasse L, Maître X. Feasibility of brain MR-elastography at 1.5 T with a novel wave generator: an animal study. In *Proceedings of the 19th Annual Meeting ISMRM*, Montreal, 2011; 3492.
 - 29 Scheffler K, Lehnardt S. Principles and applications of balanced SSFP techniques. *Eur. Radiol.* 2003; 13: 2409–2418.
 - 30 Rump J, Klatt D, Braun J, Warmuth C, Sack I. Fractional encoding of harmonic motions in MR elastography. *Magn. Reson. Med.* 2007; 57: 388–395.
 - 31 Garteiser P, Sahebjavaher RS, Beek ter LC, Salcudean S, Vilgrain V, Van Beers BE, Sinkus R. Rapid acquisition of multifrequency, multislice and multidirectional MR elastography data with a fractionally encoded gradient echo sequence. *NMR Biomed.* 2013; 26: 1326–1335.
 - 32 Brown RW, Cheng YCN, Haacke EM, Thompson MR, Venkatesan R. *Magnetic Resonance Imaging: Physical Principles and Sequence Design*. Wiley: New York; 2014.
 - 33 Sinkus R, Tanter M, Xydeas T, Catheline S. Viscoelastic shear properties of in vivo breast lesions measured by MR elastography. *Magn. Reson. Med.* 2005; 23: 159–165.
 - 34 Li W, Wu B, Liu C. Quantitative susceptibility mapping of human brain reflects spatial variation in tissue composition. *NeuroImage* 2011; 55: 1645–1656.
 - 35 Liu Y, Geever LM, Kennedy JE, Higginbotham CL, Cahill PA, McGuinness GB. Thermal behavior and mechanical properties of physically crosslinked PVA/gelatin hydrogels. *J. Mech. Behav. Biomed. Mater.* 2010; 3: 203–209.
 - 36 Ehman EC, Rossman PJ, Kruse SA, Sahakian AV, Glaser KJ. Vibration safety limits for magnetic resonance elastography. *Phys. Med. Biol.* 2008; 53: 925–935.
 - 37 Hoult DI, Richards RE. The signal-to-noise ratio of the nuclear magnetic resonance experiment. *J. Magn. Reson.* 1976; 24: 71–85.
 - 38 Koonjoo N, Parzy E, Massot P, Lepetit-Coiffé M, Marque SRA, Franconi J-M, Thiaudière E, Mellet P. *In vivo* Overhauser-enhanced MRI of proteolytic activity. *Contrast Media Mol. Imaging* 2014; 9: 363–371.
 - 39 Sarracanie M, Herisson F, Salameh N, Waddington DE, Ayata C, Rosen MS. Dynamic in vivo free radical imaging with Overhauser-enhanced MRI. In *Proceedings of the 23rd Annual Meeting ISMRM*, Toronto, 2015; 320.
 - 40 Ardenkjaer-Larsen JH, Laursen I, Leunbach I, Ehnholm G, Wistrand LG, Petersson JS, Golman K. EPR and DNP properties of certain novel single electron contrast agents intended for oximetric imaging. *J. Magn. Reson.* 1998; 133: 1–12.
 - 41 Matsumoto S, Yasui H, Batra S, Kinoshita Y, Bernardo M, Munasinghe JP, Utsumi H, Choudhuri R, Devasahayam N, Subramanian S, Mitchell JB, Krishna MC. Simultaneous imaging of tumor oxygenation and microvascular permeability using Overhauser enhanced MRI. *Proc. Natl. Acad. Sci. U. S. A.* 2009; 106: 17898–17903.
 - 42 Adhoue X, Foucher J, Laharie D, Terrebbonne E, Vergniol J, Castéra L, Lovato B, Chanteloup E, Merrouche W, Couzigou P, de Lédinghen V. Diagnosis of liver fibrosis using FibroScan and other noninvasive methods in patients with hemochromatosis: a prospective study. *Gastroenterol. Clin. Biol.* 2008; 32: 180–187.
 - 43 Paparo F, Cevasco L, Zefiro D, Biscaldi E. Diagnostic value of real-time elastography in the assessment of hepatic fibrosis in patients with liver iron overload. *Eur. J. Radiol.* 2013; 82: e755–e761.